Spread in model climate sensitivity traced to atmospheric convective mixing

Steven C. Sherwood[1], Sandrine Bony[2] and Jean-Louis Dufresne[2]

[1]*Climate Change Research Centre and ARC Centre of Excellence for Climate System Science, University of New South Wales, Sydney, Australia*

[2]*LMD/IPSL, CNRS, Université Pierre et Marie Curie, Paris, France*

Climate sensitivity refers to the change in global mean temperature in response to a change in external forcing, usually a doubling of CO_2. Despite decades of research attempting to narrow uncertainties, equilibrium climate sensitivity estimates from climate models still span roughly 2 to 5°C, precluding accurate projections of future climate. The spread arises largely from differences in the feedback from low clouds, for reasons not yet understood. Here we show that differences in the simulated strength of convective mixing between the lower and middle tropical troposphere explain about half of the variance in climate sensitivity estimated by 43 climate models. The apparent mechanism is that such mixing dehydrates the low-cloud layer at a rate that increases as climate warms, and this rate of increase depends on the initial mixing strength, linking the mixing to cloud feedback. Mixing inferred from observations appears sufficiently strong to imply a climate sensitivity greater than 3°C for a carbon dioxide doubling. This is significantly higher than the currently accepted lower bound of 1.5°C, thereby constraining model projections toward relatively severe future warming.

Introduction

Ever since numerical global climate models (GCMs) were first developed in the early 1970's they have exhibited a wide range of equilibrium climate sensitivities (roughly from 2-4.5 °C warming per equivalent doubling of CO_2)[1] and consequently broad range of future warming projections, due mostly to the range of simulated net cloud feedback[2,3]. This feedback strength varies from roughly zero in the lowest-sensitivity models to about 1.2-1.4 W m^{-2} K^{-1} in the highest[4]. High clouds (above $\sim$ 400 hPa or 8 km) contribute about 0.3-0.4 W m^{-2} K^{-1} to this predicted feedback because their top temperatures do not increase much in warmer climates, which enhances their greenhouse effect. Mid-level cloud changes also make a modest positive-feedback contribution in most models[5].

Another positive feedback in most models comes from low cloud, occurring below $\sim$750 hPa or 3 km, mostly over oceans in the planetary boundary layer below about 2 km. Low cloud is capable of particularly strong climate feedback because of its broad coverage and because its reflection of incoming sunlight is not offset by a commensurate contribution to the greenhouse effect[6]. The amount of low cloud can increase or decrease depending on the model, causing most of the overall spread in cloud feedbacks and climate sensitivities among GCMs[5,7]. No compelling theory of low cloud amount has yet emerged.

A number of competing mechanisms have however been suggested that might account for changes in either direction. On the one hand, evaporation from the oceans increases at about 2% K^{-1}, which all other things being equal may increase cloud amount[8]. On the other hand, detailed simulations of non-precipitating cloudy marine boundary layers show that if the layer deepens in a warmer climate, more dry air can be drawn down toward the surface, desiccating the layer and reducing cloud amount[8,9].

The LT-mixing mechanism and MILC

We consider that a mechanism similar to this one, which has so far been considered only for a particular cloud regime, could apply more generally to shallow upward moisture transports, e.g., by cumulus congestus clouds or larger-scale shallow overturning found broadly over global ocean regions. Air lifted out of the boundary layer can continue ascending, rain out most of its water vapour, and then return to a relatively low altitude—or it can exit directly at the low altitude, retaining much more of its initial vapour content. The latter process reduces the "bulk precipitation efficiency" of convection[10], allowing greater transport of moisture out of the boundary layer for a given precipitation rate. Such a process can increase the relative humidity above the boundary layer[11] and dry the boundary layer. Unlike the global hydrological cycle and the deep precipitation-forming circulations[12], however, it is not strongly constrained by atmospheric energetics[11].

We present measures of this Lower-Tropospheric or *LT-mixing* and the amount of moisture it transports, and show that mixing varies substantially among GCMs and that its moisture transport increases in warmer climates at a rate that appears to roughly scale with the initial LT-mixing. The resulting increase in the low-level drying caused by this mixing produces a mixing-induced low cloud (MILC) feedback of variable strength, which can explain why low-cloud feedback is typically positive[5] and why it is so inconsistent among models.

In a GCM, vertical mixing in the lower troposphere occurs in two ways (Extended Data Figure 1). First, small-scale mixing of heat and water vapour within a single grid-column of the model is implied by convective and other parametrisations. LT-mixing and associated moisture transport would depend on transport by shallow cumulus clouds, but also on the downdrafts, local compensating subsidence, and/or evaporation of falling rain assumed to accompany deeper cumulus. Second, large-scale mixing across isentropes occurs via explicitly resolved circulations. Whether this contributes to LT-mixing will again depend on model parametrisations, but in this case, on their ability to sustain the relatively shallow heating that must accompany a shallow (LT) circulation. We measure these two mixing phenomena independently, starting with the small-scale part, and show that both phenomena progressively dry the boundary layer as climate warms.

The small-scale component of LT-mixing

LT-mixing parametrised within a GCM grid cell cannot be directly diagnosed from model output (although it contributes to the convective terms in the water vapour budget, see below). We assert, however, that an atmosphere's propensity to generate it can be gauged by observing the thermal structure just above the boundary layer in ascending, raining regions. As discussed above, air there is either transported directly from the boundary layer with minimal precipitation via LT-mixing, or indirectly by ascending in deeper, raining clouds and then descending. It would arrive cool and humid in the former case, but warmer and drier in the latter case due to the extra condensation, allowing us to gauge their relative strength by observing mean-state air properties.

To do this we thus employ an index S, proportional to the differences ΔT and ΔR of temperature and relative humidity between 700 and 850 hPa (S taken as a linear combination, see Methods Summary) averaged within a broad ascending region which roughly coincides with the Indo-Pacific Warm Pool (Fig. 1). Among the full set of 48 models used in this study, those with a less negative ΔT in this region consistently show a more negative ΔR there (Fig. 2a), and the variations in each quantity are quite large. We interpret this as strong evidence that both quantities are dominated by variations, evidently large, in the amount of LT-mixing in the ascent region, with higher S indicating stronger mixing.

Small-scale LT-mixing of moisture is part of the overall source of water vapour from parametrised convection, M_{sm}. This quantity is available from nine of the models (see Methods Summary). It always exhibits strong drying near the surface. Above about 850 hPa, it can either dry the atmosphere on average or moisten it depending on the model (Extended Data Figure 2), reflecting the competition between drying from condensation and moistening from LT-mixing and from evaporating precipitation falling from higher altitudes.

Although M_{sm} does not reflect LT-mixing alone, we can test whether LT-mixing (as diagnosed from S) affects how M_{sm} responds as climate warms. The available data confirm that, upon a +4K warming, convective drying of the PBL increases by 4-17 $\mathrm{W\,m^{-2}}$ (6-30%), compared to a typical increase of 8% in global or tropical surface evaporation. The drying increase is highly correlated ($r = -0.79$) with S (Fig. 2b). Thus, convective dehydration of the PBL outstrips the increase in surface evaporation with warming, in all models except those with the lowest S. Higher-sensitivity models also have higher S (Fig. 1), suggesting that this process drives a positive feedback on climate.

The large-scale component of LT-mixing

We next turn to the large-scale LT-mixing, which we associate with shallow ascent or flows of air upward through the boundary layer top that diverge horizontally before reaching the upper troposphere. While air ascending on large scales over warm tropical oceans typically passes through nearly the whole troposphere, over cooler oceans ascent often wanes with altitude showing that this type of mixing indeed occurs in Earth's atmosphere (Fig. 3). The associated mid-level outflows are well documented for the central and eastern Pacific and Atlantic ITCZ (Intertropical Convergence Zone) and some monsoon circulations[13,14]. While these are indeed the regions where shallow ascent is steadiest, hence clearest in monthly-mean data (Fig. 3), in daily reanalysis data shallow ascent is equally strong outside the tropics due largely to contributions from extratropical storms. Note also that although we focus here on regions of ascending air, that is because the ascending branches are where the circulations are easiest to measure; they must however descend elsewhere, exerting a net transport of water vapour that is upward and toward the convective regions.

Fig. 3 compares the observations with two example models. Neither model shows as much shallow ascent (red colour) as the observation-based estimates, but the IPSL-CM5A model comes closer. While convective treatment in the newer IPSL-CM5B model is more detailed and produces better results in important respects[15], here it is seen to produce strong deep ascent (white spots) where it is weaker and shallower in observations (red zones), showing that improvement in some aspects of a simulation does not automatically generalise to others.

We quantify the large-scale LT-mixing more thoroughly by calculating the ratio D of shallow to deep overturning (see Methods Summary) in a broad region encompassing most of the persistent shallow ascent (see Fig. 3). This index D varies by a factor of four across 43 GCMs (see below). Interestingly however D and S are uncorrelated ($r = 0.01$), confirming that the two scales of mixing are controlled by different aspects of model design.

The effective source of moisture M_{LTlg} due to this shallow overturning, and its change upon climate warming, can be directly calculated from model wind and humidity fields. We approximate M_{LTlg} using monthly-mean data from the 10 available atmospheric models (see Methods Summary). Despite M_{LTlg} isolating only shallow mixing while M_{sm} includes the effects of all parameterised convection, the profiles M_{LTlg} (Fig. 4) resemble those of M_{sm}, with strong drying in the boundary layer and weak moistening above. Not unexpectedly, these effects are greater in the high-D models than in the low-D ones.

Crucially, the low-level drying also increases faster upon +4K warming in the high-D models (by about 30%, or 1.5 $\mathrm{Wm^{-2}K^{-1}}$ when expressed as a latent heat flux) than in the low-D models (25%, or 0.9 $\mathrm{Wm^{-2}K^{-1}}$). Thus the response of M_{LTlg} grows with D as M_{sm} grew with S; the relationship for D is not as strong ($r = 0.46$ land+ocean, 0.25 ocean only), partly because the spread of D happens to be somewhat narrow among the available atmosphere models, but is still significant at 95% confidence.

Climate sensitivity

We now apply the indices S and D to the 43 GCMs for which an equilibrium climate sensitivity (ECS) is available. Each index independently explains about 25% of the variance in ECS (Fig. 5a,b).

Since the ranges of D and S are similar (each 0.3-0.4), as are (approximately) those of their drying responses upon warming (see below), we form an overall LT-mixing index (the LTMI) by simply adding the two: LTMI = $S + D$. This LTMI explains about 50% of the variance in total system feedback ($r = 0.70$) and ECS ($r = 0.68$) (Fig. 5c). Thus, while our measure of LT-mixing does not explain all of the variations among GCMs, it does explain a significant portion of the model spread.

This explanatory power derives primarily from low cloud feedbacks. The correlation between LTMI and the +4K change in shortwave cloud radiative effect in the CMIP5 atmosphere models, which spans a range of 1.8 $\mathrm{W\,m^2K^{-1}}$ in the Tropics, is 0.65 in the Tropics and 0.57 in subsidence regions (equivalent values estimated from a subset of the coupled models providing the needed output are 0.25 and 0.47 respectively). These correlations suggest that the predictive skill of LTMI arises from both subsidence and other regions; further work is needed to better assess this. Cloud amount reduces more in high-LTMI models both at low and mid-levels (Extended Data Figure 3), though the greater net radiative impact of low cloud makes its effect dominate[16]. Previously reported water vapour and lapse-rate feedbacks[17] are, in constrast, not correlated with the LTMI.

Is the imputed LT-mixing impact on low clouds strong enough to explain the ~ 1.5 W m^{-2} K^{-1} spread of cloud feedbacks seen in GCMs?[4] One recent study[18] imposed increased surface latent heat fluxes in a large region typified by shallow clouds, finding an increase in cloud-related net cooling of about 1 Wm^{-2} for a 2-3 Wm^{-2} increase in the surface flux, other things held fixed. An even larger sensitivity, nearly 1:1, has been reported in a different model for advective changes in moisture input[19]. If a similar but opposite cloud response occurred for moisture removal by LT-mixing, then to explain the feedback spread, the boundary-layer drying responses would need to span a range across models of about 3 W m^{-2} per K of surface warming. This roughly matches the contribution to the spread from $M_{\rm sm}$ alone (Fig. 2b). The additional drying response from $M_{\rm LTlg}$ was about 0.6 W m^{-2} K^{-1} greater in the high-D models (mean D of 0.34) than in the low-D ones (mean 0.24), which if rescaled by the full spread of D in the full GCM ensemble, implies a further source of spread in drying response of about 2 W m^{-2} K^{-1}. We conclude that, even if not all low clouds are as sensitive as the ones examined in the cited studies, the LT-mixing response is strong enough to account for the cloud feedback spread and its typically positive sign[5].

Why does moisture transport increase so strongly with warming? The magnitude of these increases, typically 5-7% K^{-1}, is roughly what would be expected if the circulations remained similar against a Clausius-Clapeyron increase in moisture gradients[20], as indeed it does, at least for the large-scale part[21] (Extended Data Figure 4). Further study is needed to understand why this is so, and to examine in greater detail how clouds respond to changing moisture transports; changes in low cloud amount may for example help the atmosphere restore imbalances in boundary layer moist enthalpy such as those caused by LT-mixing[19]. Since LTMI ignores any information on clouds, it is likely that additional measures of cloud characteristics[22] could explain some of the variations in low-cloud feedback not yet explained here.

We end by considering observational estimates of S and D (see Fig. 5). These show an S near the middle of the GCM range, but a D close to the top end, as hinted already by Fig. 3. D may not be well constrained since ω must be inferred from observational reanalyses, although available horizontal wind observations support the existence of strong mid-level outflows[13], and the result is consistent across both reanalyses examined. The reanalysis estimates of S are less consistent but this quantity can be fairly well constrained by radiosonde observations.

Taking the available observations at face value implies a most likely climate sensitivity of about 4°C, with a lower limit of about 3 °C. Indeed, all 15 of the GCMs with ECS below 3.0 °C have an LTMI below the bottom of the observational range. Further work may be needed to better constrain these indices, and to test whether their relationship to ECS is robust to design factors common to all models. For example this should be tested in global cloud-resolving models. The possibility can never be ruled out that feedbacks could exist in nature that are missing from all models, which would change the climate sensitivity from that suggested by our result. Nonetheless, based on the available data, the new understanding presented here pushes the likely long-term global warming toward the upper end of model ranges.

Discussion

While a few previous studies have already noted that higher-sensitivity models better simulate certain cloud-relevant phenomena[23–25], ours is the first to demonstrate a causal physical mechanism, or to show consistent predictive skill across so many models, or to point to processes connecting low-cloud regions to the deep tropics. The MILC mechanism is surprisingly straightforward. LT-mixing dries the boundary layer, and the drying rate increases by 5-7% K^{-1} in warmer climates due to stronger vertical water vapour gradients. The moisture source from surface evaporation increases at only about 2% K^{-1}. Thus as climate warms, any drying by LT-mixing becomes larger relative to the rest of the hydrological cycle, tending to dry the boundary layer. How important this is depends on how important the diagnosed LT-mixing was in the base state of the atmosphere. LT-mixing is unrealistically weak in models that have low climate sensitivity.

Climate-sensitivity-related differences in LT-mixing, both at small (Fig. 1) and large scales (Fig. 3), are most detectable in regions of tropical deep or mixed-level convection and mean upward motion. This does not mean, however, that the greater low-level drying in a warmer climate or its spread among models will be limited to these regions. Large-scale LT-mixing carries water vapour not only upward but also horizontally away from subsidence regions; since both directions of transport intensify in a warmer atmosphere[20], subsidence regions should bear the brunt of the overall boundary-layer drying. Moreover, shallow ascent is equally strong (though more transient) in mid-latitude storm tracks as in the tropics, suggesting that MILC feedback may be just as important outside the tropics as in them. As for small-scale LT mixing, even though there are reasons to measure it in ascending regions (see Methods), its impact upon warming is much more widespread and differs significantly among models in subsiding regions (Extended Data Figure 5). We hypothesise that this is because models with more small-scale LT-mixing in ascending regions also have more in descending regions, although we cannot directly confirm this. Overall the behaviour is consistent with published results showing that subsiding regions contribute strongly to the spread of cloud feedbacks in models, with storm tracks and tropical convective regions also playing a role[16,26,27].

LT-mixing behaviour appears to result from a competition between shallow and deep convection in situations where either could occur. Such situations persist in many tropical regions, notably the ITCZ. Understanding and properly representing this competition in climate models is undoubtedly needed for more accurate future climate projections.

Although tested here on models used over the past decade or so, we presume that this mechanism has been a leading source of spread in sensitivity since the dawn of climate modelling. To finally identify an atmospheric process that drives variations in climate sensitivity offers an unprecedented opportunity to focus research and model development in ways that should lead to more reliable climate change assessments.

Methods Summary

Data for computing S and D come from control runs of 48 models: 18 from CMIP3 (Coupled Model Intercomparison Project version 3)[28] and 30 from CMIP5[29] (see Extended Data Tables 1-2).

ECS was reported for all but one CMIP3 model by the IPCC[28]. For CMIP5 we employ effective climate sensitivities calculated from abrupt 4xCO_2 experiments, available for 26 models, following a standard regression procedure[30,31]. Data for $M_{\rm sm}$ and $M_{\rm LTlg}$ come from 10 CMIP5 atmosphere models providing "amip" (specified ocean surface temperature) control and +4K ocean warming runs. Eight of these models provided $M_{\rm sm}$; we also included data from the PCM (CMIP3).

Observational estimates come from radiosondes and two monthly reanalysis products (ERAi and MERRA). Reanalyses are produced from a model constrained to the full extent possible by a variety of observations[32,33].

We calculate S within a region where convective effects are a leading term in thermodynamic budgets, defined by the upper quartile of the annual-mean mid-tropospheric ascent rate where it is upward, $-\omega_{500}$ (ω the pressure velocity). We define $S \equiv (\Delta R/100\% - \Delta T/9\text{K})/2$, which normalises ΔR to 100% humidity, ΔT to the $\sim$ 9K range between dry and saturated adiabatic values, and averages these two pieces of information with equal weight to reduce noise from other factors.

To calculate $M_{\rm LTlg}$ we compute ω_1 (the average of ω at 850 and 700 hPa) and ω_2 (the average among 600, 500 and 400 hPa). $\Delta = \omega_2 - \omega_1$ measures the local horizontal outflow in the lower troposphere above the boundary layer. Moisture is transported upward and outward wherever $\Delta > 0$ and $\omega_1 < 0$. We restrict measurement to tropical ocean regions from 160W-30E (see Fig. 3). The moisture supplied to the environment is estimated as $M_{\rm LTlg} = -\langle q\, d\omega/dp\, H(\Delta) H(-\omega_1)\rangle$, where q is the specific humidity, $\langle\rangle$ a mean over the restricted region, and H the step function.

Finally $D \equiv \langle \Delta\, H(\Delta)\, H(-\omega_1) \rangle / \langle -\omega_2\, H(-\omega_2) \rangle$.

1. Hegerl, G. C. & Zwiers, F. W. *Working Group I: The physical science basis of climate change*, chap. 9. Understanding and Attributing Climate Change, 663–745 (Cambridge University Press, 2007).

2. Cess, R. D. *et. al*. Intercomparison and interpretation of climate feedback processes in 19 atmospheric general circulation models. *J. Geophys. Res.* **95**, 16,601–16,615 (1990).

3. Dufresne, J. L. & Bony, S. An assessment of the primary sources of spread of global warming estimates from coupled atmosphere-ocean models. *J. Climate* **21**, 5135–5144 (2008).

4. Soden, B. J. *et al.* Quantifying climate feedbacks using radiative kernels. *J. Climate* **21**, 3504–3520 (2008).

5. Zelinka, M., Klein, S. & Hartmann, D. Computing and partitioning cloud feedbacks using cloud property histograms. Part I: Cloud radiative kernels. *J. Climate* **25**, 3715–3735 (2012).

6. Hartmann, D. L. & Short, D. A. On the use of earth radiation budget statistics for studies of clouds and climate. *J. Atmos. Sci.* **37**, 1233–1250 (1980).

7. Bony, S. & Dufresne, J. L. Marine boundary layer clouds at the heart of tropical cloud feedback uncertainties in climate models. *Geophys. Res. Lett.* **32**, L20806 (2005).

8. Rieck, M., Nuijens, L. & Stevens, B. Marine boundary-layer cloud feedbacks in a constant relative humidity atmosphere. *J. Atmos. Sci.* **69**, 25382550 (2012).

9. Stevens, B. On the growth of layers of nonprecipitating cumulus convection. *J. Atmos. Sci.* **64**, 2916–2931 (2007).

10. Yano, J. & Emanuel, K. An improved model of the equatorial troposphere and its coupling with the stratosphere. *J. Atmos. Sci.* **48**, 377–389 (1991).

11. Sherwood, S. C. & Meyer, C. L. The general circulation and robust relative humidity. *J. Climate* **19**, 6278–6290 (2006).

12. Allen, M. R. & Ingram, W. J. Constraints on future changes in climate and the hydrologic cycle. *Nature* **419**, 224–232 (2002).

13. Zhang, C. D., Nolan, D. S., Thorncroft, C. D. & Nguyen, H. Shallow meridional circulations in the tropical atmosphere. *J. Climate* **21**, 3453–3470 (2008).

14. Nolan, D. S., Powell, S. W., Zhang, C. D. & Mapes, B. E. Idealized simulations of the Intertropical Convergence Zone and its multilevel flows. *J. Atmos. Sci.* **67**, 4028–4053 (2010).

15. Rio, C., Hourdin, F., Grandpeix, J. Y. & Lafore, J. P. Shifting the diurnal cycle of parameterized deep convection over land. *Geophys. Res. Lett.* **36**, L07809 (2009).

16. Soden, B. J. & Vecchi, G. A. The vertical distribution of cloud feedback in coupled ocean-atmosphere models. *Geophys. Res. Lett.* **38**, L12704 (2011).

17. Soden, B. J. & Held, I. M. An assessment of climate feedbacks in coupled ocean-atmosphere models. *J. Climate* **19**, 3354–3360 (2006).

18. Webb, M. & Lock, A. Coupling between subtropical cloud feedback and the local hydrological cycle in a climate model. *Clim. Dyn.* 10.1007/s00382–012–1608–5 (2012).

19. Brient, F. & Bony, S. Interpretation of the positive low-cloud feedback predicted by a climate model under global warming. *Climate Dynamics* **40**, 2415–2431 (2012).

20. Held, I. M. & Soden, B. J. Robust responses of the hydrological cycle to global warming. *J. Climate* **19**, 5686–5699 (2006).

21. Zahn, M. & Allan, R. P. Climate warming - related strengthening of the tropical hydrological cycle. *J. Climate* **26**, 562–574 (2013).

22. Klein, S. A. *et al.* Are climate model simulations of clouds improving? An evaluation using the ISCCP simulator. *J. Geophys. Res.* **118**, 1329–1342 (2013).

23. Volodin, E. M. Relation between temperature sensitivity to doubled carbon dioxide and the distribution of clouds in current climate models. *Izvestiya Atmospheric and Oceanic Physics* **44**, 288–299 (2008).

24. Clement, A. C., Burgman, R. & Norris, J. R. Observational and model evidence for positive low-level cloud feedback. *Science* **325**, 460–464 (2009).

25. Fasullo, J. T. & Trenberth, K. E. A less cloudy future: The role of subtropical subsidence in climate sensitivity. *Science* **338**, 792–794 (2012).

26. Webb, M. J., Lambert, F. H. & Gregory, J. M. Origins of differences in climate sensitivity, forcing and feedback in climate models. *Clim. Dyn.* **40**, 677–707 (2013).

27. Vial, J., Dufresne, J.-L. & Bony, S. On the interpretation of inter-model spread in CMIP5 climate sensitivity estimates. *Clim. Dyn.* In Press (2013).

28. Randall, D. A. & Wood, R. A. *Working Group I: The physical science basis of climate change*, chap. 8. Climate models and their evaluation, 589–662 (Cambridge University Press, 2007).

29. Taylor, K. E., Stouffer, R. J. & Meehl, G. A. An overview of CMIP5 and the experiment design. *Bull. Amer. Meteorol. Soc.* **93**, 485–498 (2012).

30. Gregory, J. M. *et al.* A new method for diagnosing radiative forcing and climate sensitivity. *Geophys. Res. Lett.* **31**, L03205 (2004).

31. Forster, P. M. *et al.* Evaluating adjusted forcing and model spread for historical and future scenarios in the CMIP5 generation of climate models. *J. Geophys. Res.* (2013). Doi:10.1002/jgrd.50174.

32. Uppala, S. M. & Coauthors. The ERA-40 re-analysis. *QJRMS* **131**, 2961–3012 (2005).

33. Rienecker, M. M. & CoAuthors. MERRA: NASA's modern-era retrospective analysis for research and applications. *J. Climate* **24**, 3624–3658 (2011).

34. Sherwood, S. C., Meyer, M. L., Allen, R. J. & Titchner, H. A. Robust tropospheric warming revealed by iteratively homogenized radiosonde data. *J. Climate* **21**, 5336–5352 (2008).

35. Sherwood, S. C., Roca, R., Weckwerth, T. M. & Andronova, N. G. Tropospheric water vapor, convection and climate. *Rev. Geophys.* **48** (2010). Doi:10.1029/2009RG00030, RG2001.

Acknowledgements This work was supported by the FP7-ENV-2009-1 European project EUCLIPSE (#244067). We acknowledge the World Climate Research Programme's Working Group on Coupled Modelling, which is responsible for CMIP, and we thank the climate modelling groups for producing and making available their model output, especially the participants contributing additional CFMIP2 experiments and diagnostics crucial to our study. The U.S. Department of Energy's Program for Climate Model Diagnosis and Intercomparison provides coordinating support for CMIP and led development of software infrastructure in partnership with the Global Organisation for Earth System Science Portals. We also thank the National Center for Atmospheric Research and the Earth System Grid Federation for providing access to PCM output, the Australian National Computational Infrastructure, the IPSL Prodiguer-Ciclad facility for providing a convenient archive of CMIP data. Finally we thank B. Stevens, C. Bretherton and G. Schmidt for comments on early versions of the manuscript.

Author Contributions SCS led the study and the writing of the paper, and did the calculations of LTMI and related diagnostics. SB computed cloud radiative effect and assisted in interpreting results and writing the paper. JLD computed ECS and assisted in interpreting results and writing the paper.

Methods

Data for computing S and D come from 48 models: 18 from the CMIP3 (Coupled Model Intercomparison Project version 3)[28], first two years of each "picntrl" run, and 30 models from the CMIP5[29], first two years of each "1pctCO2" run. Two years of data is sufficient to specify S and D to within 0.02 or better of their long-term values. CMIP3 data were obtained from the Australian NCI node, and CMIP5 data including the amip and amip+4K runs were obtained on 14/9/2012 and 22/10/2012 from the IPSL Ciclad repository. ECS values for CMIP3 were reported for all but one model by the IPCC[28]. For CMIP5 we employ effective climate sensitivities calculated from abrupt $4xCO_2$ experiments, available for 26 of the 30 CMIP5 models, following a standard regression procedure[30,31].

Data for M_{sm} and M_{LTlg} come from 10 CMIP5 atmosphere models providing "amip" (specified ocean surface temperature) control and +4K ocean warming experiments. A key advantage of this experiment setup is that interannual ocean variability is the same in the control and warming runs, and changes in the SST pattern, which could complicate interpretation especially for circulation changes, are avoided. Data are from 1989-98, except for IPSL-CM5A where some of these years were corrupted and alternative years were used. Results from individual years were similar to those for the 10-year averages. Eight of these models provided M_{sm}; we also included data from the PCM CMIP3 1%-per-year-to-quadrupling experiment, with changes rescaled to +4K equivalent (actual change 3.3K). PCM M_{sm} data come from 10 years near the beginning and 10 near the end of the 1%-per-year-to-quadrupling experiment, obtained from the NCAR node of the ESG.

Shortwave cloud radiative effect (SWCRE) is obtained by differencing the all-sky and clear-sky top-of-atmosphere shortwave fluxes for each model run. To calculate cloud feedback we first composite the sensitivity of SWCRE to SST in dynamical regimes defined by vertical-mean vertical velocity, and then we compute the sum (weighted by the PDF of omega) over regimes (or only subsidence regimes defined by $\omega > 0$)[7]. For coupled models, the warming-induced change is obtained from abrupt CO_2 quadrupling experiments, after removing the instantaneous change associated with rapid adjustment to higher CO_2 estimated from the first 12 months after quadrupling.

Only one realisation is used per model. For atmosphere-only models it is simply the difference between +4K and control simulations.

Observational estimates come from radiosondes and from two monthly reanalysis products (ERAi and MERRA), years 2009-10. The reanalyses are produced from a model constrained to the full extent possible by a variety of observations[32,33]. MERRA reanalysis data from 1 September 2009 were used to compare D inside/outside the Tropics, but monthly data were used otherwise. Radiosonde data were obtained from the IGRA archive and subjected to simple quality-control checks for outliers. The 10 stations sited in the relevant region and meeting the criteria described by a previous study[34] were used, and the mean taken over the two years. The radiosonde network sampling bias, as determined from station-sampled reanalysis output, was relatively small compared to the overall reanalysis biases.

We calculate S in ascending regions, where convective effects are a leading term in thermodynamic budgets; in subsidence regions humidity is sensitive to irrelevant non-local factors and even to numerical resolution[35], perhaps explaining why it is less informative for our purposes. The calculation region is defined by the upper quartile of the annual-mean mid-tropospheric ascent rate in ascending regions, $-\omega_{500}$ (ω the pressure velocity). We define $S \equiv (\Delta R/100\% - \Delta T/9\mathrm{K})/2$, which normalises ΔR to 100% humidity, ΔT to the ~ 9K range between dry and saturated adiabatic values, and then averages these two pieces of information with equal weight. Such averaging should reduce the noise from other factors that influence one quantity or the other. Varying the weighting of the two terms does not strongly affect results.

To calculate M_{LTlg}, we first compute ω_1 (the average ω at 850 and 700 hPa) and ω_2 (the average among 600, 500 and 400 hPa). The difference $\Delta = \omega_2 - \omega_1$ then measures the local horizontal outflow in the lower troposphere above the boundary layer. Moisture is transported upward and outward at this level wherever $\Delta > 0$ and $\omega_1 < 0$. We restrict measurement to tropical ocean regions from 160W-30E (see Fig. 3). The moisture supplied to the environment is then estimated as $M_{\mathrm{LTlg}} = -\langle q\, d\omega/dp\, H(\Delta)H(-\omega_1)\rangle$, where q is the specific humidity, $\langle\rangle$ indicates the mean over the restricted calculation region, and H is the step function. The index D is computed as $D \equiv \langle\Delta\, H(\Delta)\, H(-\omega_1)\rangle / \langle -\omega_2\, H(-\omega_2)\rangle$.

Values of D and S are similar with 10 years of data or one year, and are similar whether individual months or long-term means for each month of the year are used. These indices capture over 25% of the ECS variance even if computed from only a single month of data from each model. Thus, long records are unnecessary for deducing the strength of LT-mixing.

The reason for restricting calculation of D to the cooler tropical longitudes is that a few climate models erroneously place much of the shallow ascent over warm oceans, where it does not seem to contribute as much to low-cloud feedback. In observations, and in most models, the restriction has little effect since most of the shallow ascent persistent enough to appear in monthly-mean data is already located in the specified region. We speculate that the location of the ascent matters because the associated shallow descent is more relevant if it occurs over, or upstream of, regions of radiatively important low cloud.

Both LT-mixing indices retain statistically significant correlations with ECS for all alterations to their definitions that we tried. Specifically, the correlation of S with ECS ($r_{S-\mathrm{ECS}}$) is similar with ω_{500} percentiles of 0.25 or 0.5, but drops with looser thresholds, which begin to pick up parts of the resolved LT-mixing region. Tighter thresholds reduce the spread in S between models, reducing $r_{S-\mathrm{ECS}}$. The correlation $r_{D-\mathrm{ECS}}$ is somewhat weaker (as low as 0.3) if the longitudinal restriction for D is removed, or if other definitions of ω_1 and ω_2 are used.

Figure 1 Multimodel-mean local stratification parameter s. The index S is the mean of s within the regions outlined in white. Multimodel averages of s are shown separately for (**a**) low-sensitivity (ECS $<$ 3.0 °C) and (**b**) high-sensitivity (ECS $>$ 3.5 °C) models, among coupled models with known ECS. The white dots inside the S-averaging region show locations of radiosonde stations used to help estimate S observationally. A few coastal regions that are off-scale appear white.

Figure 2 Basis for the index S **of small-scale LT-mixing and its relationship to the warming response.** (**a**) $\Delta T_{700-850}$ vs. $\Delta R_{700-850}$, each averaged over a tropical region of mean ascent (see Fig. 1), from all 48 coupled models; for reference, a saturated-adiabatic value of ΔT is shown by dotted line, and a dry-adiabatic value (not shown) would be ~ -16K. Error bars are 2-σ ranges. (**b**) Change in small-scale moisture source M_{sm} below 850 hPa in the Tropics upon +4K ocean warming, vs. S computed from the control run, in eight atmosphere models and one CMIP3 model. Symbol colour indicates modelling centre or centre where atmosphere model was originally developed (see legend), shape indicates model generation.

Figure 3 The structure of monthly-mean tropospheric ascent reveals large-scale LT-mixing in observations and models. Upward pressure velocity in one September month from (**a**) the MERRA reanalysis, (**b**) IPSL-CM5A model and (**c**) IPSL-CM5B model, with values at 850 hPa shown in red and those at 500 hPa shown in green plus blue. Bright red implies ascent that is weighted toward the lower troposphere with mid-tropospheric divergence (see colour scale), white implies deep ascent, and dark colours imply descent. In (**a**) black lines outline the region in which the index D of large-scale LT-mixing is computed. The Pacific and Atlantic ITCZ regions are consistently red in the reanalyses and models, while isolated red patches in other areas tend to vary with time.

Figure 4 Estimated water vapour source M_{LTlg} due to large-scale LT-mixing and its response to warming. See Methods for calculation details. Data are from 10 CMIP5 atmosphere models, averaged 30S-30N over oceans, with the average of the four models having largest D shown in magenta and that of the four with smallest D shown in blue. Dashes show results in +4K climate. Changes at +4K are nearly identical whether or not land areas are included.

Figure 5 Relation of LT-mixing indices to Equilibrium climate sensitivity (ECS). ECS vs. (**a**) S, (**b**) D, and (**c**) LTMI = $S + D$ from the 43 coupled models with known ECS. Linear correlation coefficients are given in each panel (second figure in bottom panel is the correlation to total system feedback). Error bars shown near panel axes indicate 2σ ranges of: (**a**) the direct radiosonde estimate, (**c**) the S from radiosondes added to the D from each of the two reanalyses.

Extended Data Figure 1 — Illustration of atmospheric overturning circulations. Deep overturning strongly coupled to the hydrological cycle and atmospheric energy budget is shown by solid lines; LT-mixing is shown by dashed lines. The MILC feedback results from the increasing relative role of LT-mixing in exporting humidity from the boundary layer as climate warms, thus depleting the layer of water vapour needed to sustain low cloud cover.

Extended Data Figure 2 — Small-scale moisture source M_{sm}. Vertical profile averaged over all tropical oceans, for two selected climate models (see legend) with very different warming responses, in present-day (solid) and +4K (dashed) climates.

Extended Data Figure 3 — Response of cloud fraction to warming. Profile of average change in model cloud fractional cover at +4K in the four atmosphere models with largest (magenta) and smallest (blue) estimated +4K increases in PBL drying, averaged from 30S-30N (dashed) or 60S-60N (solid). Drying estimate is obtained by adding the explicitly computed change in M_{lg} to the change in M_{sm} estimated from S via the relationship shown in Fig. 2a. Typical mean cloud fraction below 850 hPa is about 10-20%, and the changes shown are absolute changes in this fraction, so are of order 10% of the initial cloud cover.

Extended Data Figure 4 — Response of large-scale LT-mixing to warming. Profiles of mean vertical velocity in regions of shallow ascent, in control and +4K climates. Similarity of dashed and solid lines indicates that mass overturning associated with these regions is roughly the same in the warmer simulations, on average.

Extended Data Figure 5 — Response of small-scale, low-level drying to warming. Change in convective moisture source $M_{\rm sm}$ below 850 hPa upon a +4K warming in eight atmosphere models and one CMIP3 coupled model; units are $\rm W\,m^{-2}$, with negative values indicating stronger drying near the surface. Zero contours are shown in white (a few off-scale regions also appear white). The models used for calculating $M_{\rm lg}$ are the eight shown here plus two for which $M_{\rm sm}$ data were unavailable: CNRM-CM5 and FGOALS-g2.

Model	Centre	Forcing (W m^2)	Total feedback (W m$^2 K^{-1}$)	ECS (K)
ACCESS1-0	ACCESS	3.01	-0.79	3.79
ACCESS1-3	ACCESS	2.96	-0.86	3.45
BCC-CSM1-1	BCC	3.35	-1.16	2.88
BNU-ESM	GCESS/BNU	3.78	-0.92	4.11
CanESM2	CCC	3.85	-1.05	3.68
CCSM4	NCAR	3.70	-1.27	2.92
CESM1-BGC	NCAR	—	—	—
CESM1-CAM5	NCAR	—	—	—
CMCC-CM	CMCC	—	—	—
CNRM-CM5	CNRM	3.71	-1.14	3.25
CSIRO-Mk3-6-0	CSIRO/QCCCE	2.63	-0.66	3.99
FGOALS-g2	LASG/IAP	2.89	-0.84	3.45
FGOALS-s2	LASG/IAP	3.84	-0.92	4.16
GFDL-CM3	GFDL	3.00	-0.76	3.96
GFDL-ESM2G	GFDL	3.11	-1.31	2.38
GFDL-ESM2M	GFDL	3.41	-1.41	2.41
GISS-E2-H	GISS	3.83	-1.66	2.30
GISS-E2-R	GISS	3.77	-1.79	2.11
HadGEM2-ES	MOHC	2.95	-0.65	4.55
INMCM4	INM	2.98	-1.44	2.07
IPSL-CM5A-LR	IPSL	3.12	-0.76	4.10
IPSL-CM5B-LR	IPSL	2.66	-1.03	2.59
MIROC5	MIROC	4.16	-1.54	2.71
MIROC-ESM	MIROC	4.27	-0.92	4.65
MPI-ESM-LR	MPI	4.15	-1.15	3.60
MPI-ESM-MR	MPI	4.11	-1.20	3.44
MPI-ESM-P	MPI	4.35	-1.27	3.42
MRI-CGCM3	MRI	3.26	-1.26	2.59
NorESM1-ME	NCC	—	—	—
NorESM1-M	NCC	3.21	-1.13	2.83

Extended Data Table 1 — List of CMIP5 coupled models used. Centre acronyms used to identify them in scatter plots are also shown. The derived forcing, total feedback, and equilibrium climate sensitivities are given for models with abrupt 4xCO_2 simulations.

Model	Centre	ECS (K)
CCCMA-CGCM3 1	CCC	3.4
CCCMA-CGCM3 1 T63	CCC	3.4
GFDL-CM2-0	GFDL	2.9
GFDL-CM2-1	GFDL	3.4
GISS-MODEL-E-H	GISS	2.7
GISS-MODEL-E-R	GISS	2.7
IAP-FGOALS1-0-G	IAP	2.3
INGV-ECHAM4	INGV	—
INMCM3-0	INM	2.1
IPSL-CM4	IPSL	4.4
MIROC3-2-HIRES	MIROC	4.3
MIROC3-2-MEDRES	MIROC	4.0
MPI-ECHAM5	MPI	3.4
MRI-CGCM2-3-2A	MRI	3.2
NCAR-CCSM3-0	NCAR	2.7
NCAR-PCM1	NCAR	2.1
UKMO-HadCM3	MOHC	3.3
UKMO-HadGEM1	MOHC	4.4

Extended Data Table 2 — List of CMIP3 coupled models used. Centre acronyms used to identify them in scatter plots are also shown, as are feedback values given by Randall et al. (2007).

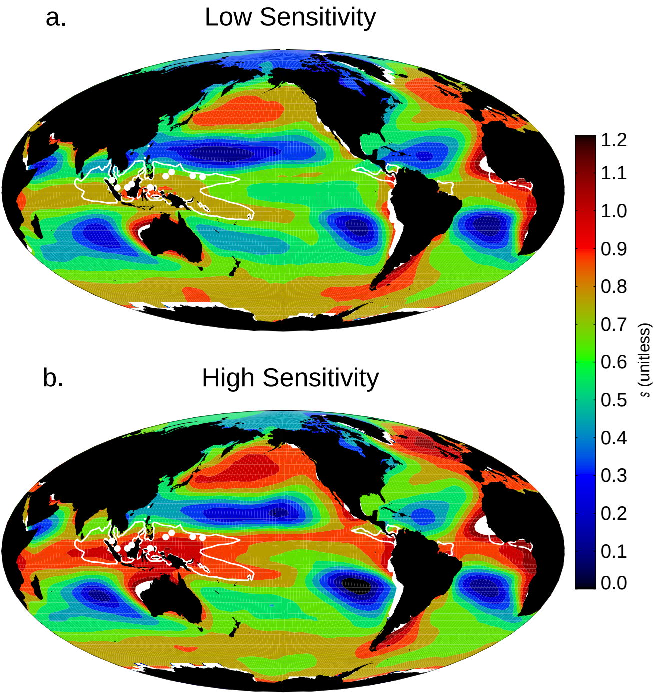

a.
Low Sensitivity
b.
High Sensitivity
1.2
1.1
1.0
0.9
0.8
0.7
0.6
0.5
0.4
0.3
0.2
0.1
0.0
s (unitless)

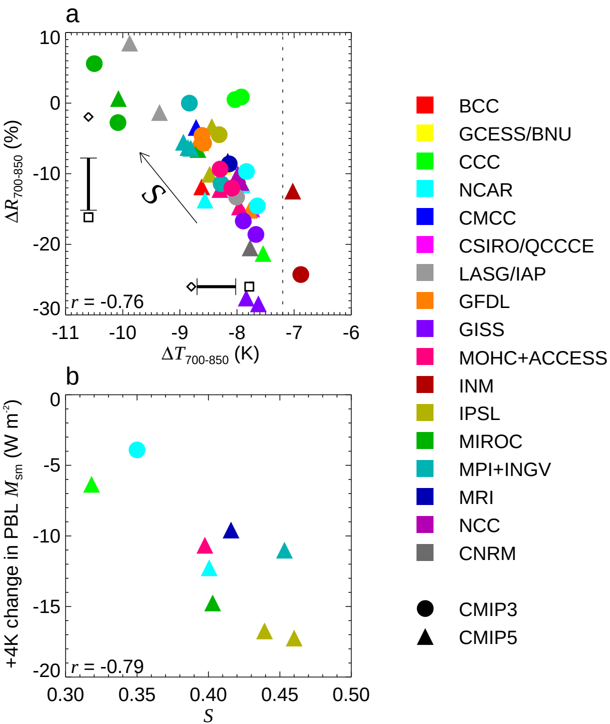
a
r = -0.76
S
ΔR700-850 (%)
ΔT700-850 (K)
b
r = -0.79
+4K change in PBL Msm (W m-2)
S
BCC
GCESS/BNU
CCC
NCAR
CMCC
CSIRO/QCCCE
LASG/IAP
GFDL
GISS
MOHC+ACCESS
INM
IPSL
MIROC
MPI+INGV
MRI
NCC
CNRM
CMIP3
CMIP5

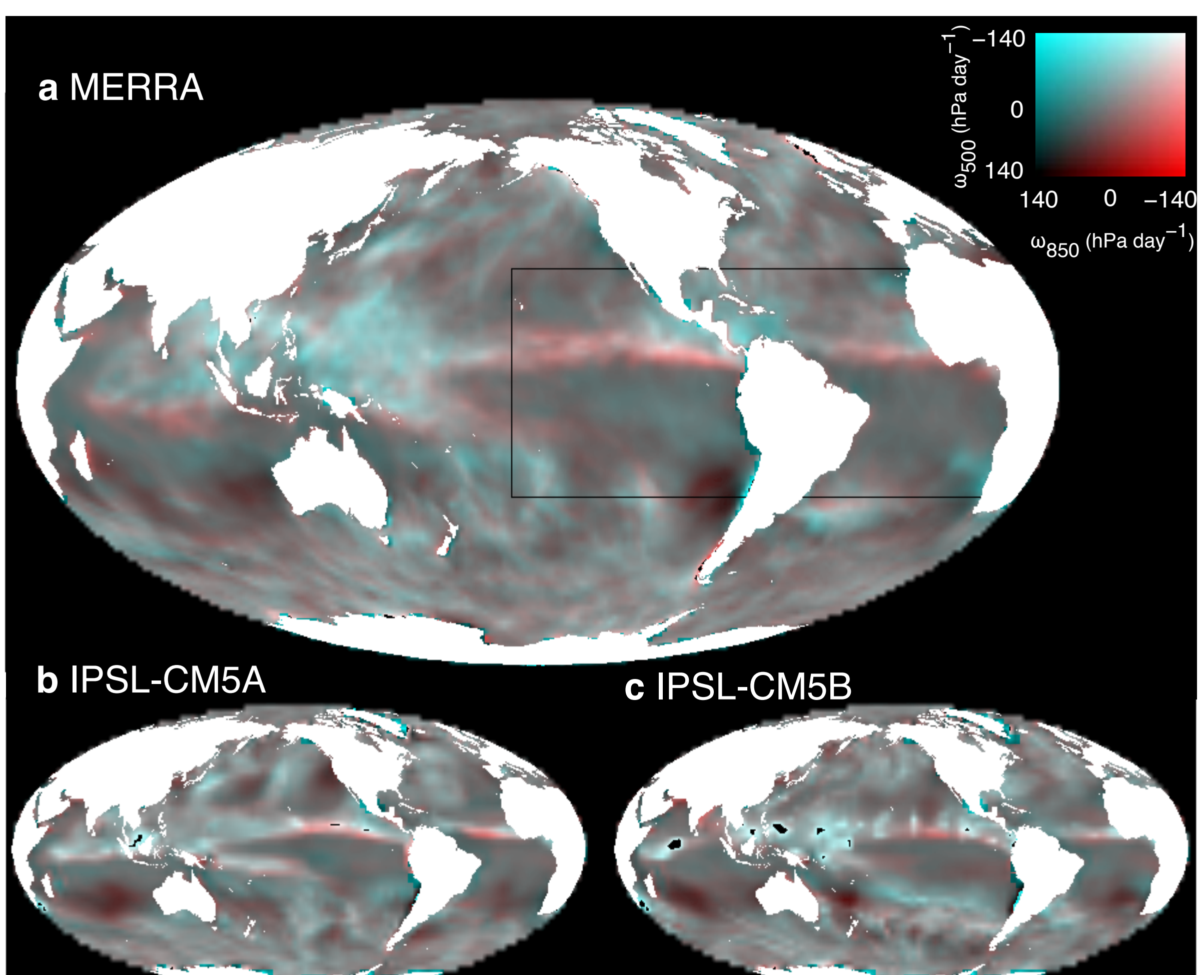
a MERRA
b IPSL-CM5A
c IPSL-CM5B
−140
0
140
140
0
−140
ω_{500} (hPa day^{-1})
ω_{850} (hPa day^{-1})

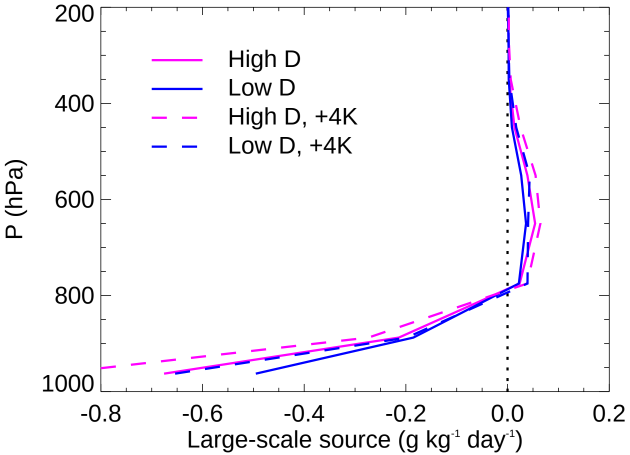

200
400
600
800
1000
P (hPa)
High D
Low D
High D, +4K
Low D, +4K
-0.8
-0.6
-0.4
-0.2
0.0
0.2
Large-scale source (g kg-1 day-1)

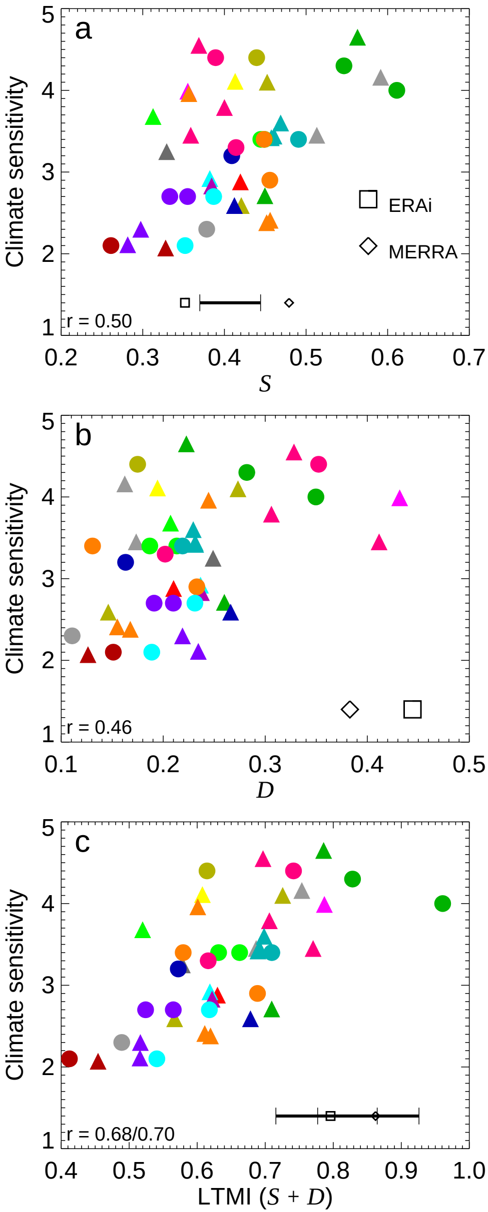

a
Climate sensitivity
S
ERAi
MERRA
r = 0.50
b
D
r = 0.46
c
LTMI (S + D)
r = 0.68/0.70